

Influence of Particle Size Distribution on the Morphology and Cavitation Resistance of High-Velocity Oxygen Fuel Coatings

L. L. Silveira¹ · G. B. Sucharski² · A. G. M. Pukasiewicz¹ · R. S. C. Paredes²

Submitted: 19 April 2017 / in revised form: 7 February 2018 / Published online: 28 February 2018
© ASM International 2018

Abstract The cavitation wear process is one of the major wear mechanisms in turbines and rotors of hydroelectric power plants in Brazil. An effective way to increase the cavitation resistance is the use of coatings, applied by thermal spraying. The high-velocity oxy-fuel process (HVOF) is one of the most used thermal spraying processes, and it is widely adopted for applying coatings for protection against wear and in maintenance components. A FeCrMnSiB experimental alloy was deposited onto SAE 1020 substrate by HVOF process, in order to evaluate the influence of the powder particle size range on the morphology and cavitation resistance of the coatings. The morphology of the coatings showed an increase in oxide content with powder size reduction. The increase in the powder particle size reduced the wettability of the particles, observed by the increase in the quantity of non-melted particles. Higher particle size distribution led to an increase in erosion rate, due to higher presence of non-melted particles in the coatings and consequently reduction of splats adhesion. The cavitation damage was perceived mainly by the mechanism of lamellae detachment; however, part of the damage was also absorbed by strain hardening due to the γ - ϵ martensitic transformation.

Keywords Fe-based alloy · particle size · protective coatings · thermal spray

Introduction

Cavitation erosion is the mechanical degradation and mass loss damage due to the repetitive nucleation, growth and collapse of bubbles in a fluid. The generation of shock waves or microjets during the collapse of bubbles is the mechanisms proposed to explain the cavitation damage in solid surfaces. In both cases, the mechanical loads are very localized and repetitive, resulting in surface deformation and erosion (Ref 1-4). Cavitation is a common problem in hydroelectric power plants, leading to reduction in the efficiency, maintenance costs increase and reduction in productive capacity (Ref 5-7).

Fe-Mn-Si alloys have low stacking-fault energy (SFE), and the dominant deformation mechanism is the formation of stacking faults, regarded as the embryos of ϵ -martensite. Decreased SFE is known to promote strain-induced martensitic transformations, promoting strain hardening and consequently higher strain energy absorption (Ref 8-14). Alloys with low values of SFE are known to have superior cavitation resistance than alloys without strain-induced phase transformation, or than alloys which presented only the γ - α' phase transformation (Ref 4, 15). The formation of ϵ -martensite in the vicinity of grain boundaries and α' -martensite in the interior of grains led to excellent cavitation erosion resistance (Ref 16).

Surface properties have been studied to improve cavitation resistance (Ref 3), as well as the use of coatings applied by various deposition methods, such as arc welding (Ref 17), plasma spray (Ref 18), thermal spray (Ref 19), and other techniques (Ref 20, 21). Thermal spray techniques have been widely used and are considered the most effective and practical solution, due to its variety of coating material choice, shape and size of the applied surfaces and minor modification of the properties of the substrate (Ref

✉ L. L. Silveira
luciana.lsilveira@gmail.com

¹ Post-graduate Program in Mechanical Engineering, Federal University of Technology - Parana, Ponta Grossa, PR, Brazil

² Post-graduate Program in Mechanical Engineering, Federal University of Paraná, Curitiba, PR, Brazil

3, 22, 23). The adhesion bond strength in thermal spray is related to the mechanical anchoring mechanisms (Ref 24), and the role of particle size in creating a coating with superior cavitation resistance is intimately related to the particle adherence on the substrate, with consequent superior adhesion bond strength.

The high-velocity oxy-fuel (HVOF) thermal spray process uses the thermal energy, produced by the combustion of fuel with oxygen, to heat and propel the powder particles. HVOF has been widely used to deposit a large variety of metal and cermet coatings, modifying the surface properties of the substrate (Ref 25), to form protective coatings against wear (under sliding stress) (Ref 26), corrosion (Ref 26, 27) and also cavitation erosion (Ref 4, 19, 28).

The study of the particle characteristics is of great importance to understand its influence on the morphology and properties of the HVOF-sprayed coatings. Variables such as particle temperature (Ref 29–31), velocity (Ref 19, 29–31), morphology (Ref 32) and size (Ref 33–35) have been extensively studied, providing better understanding of their effects on the morphology, porosity, oxidation and mechanical properties of the HVOF coatings.

Rajasekaran et al. (Ref 33) studied the influence of oxy-fuel ratio (O_2/H_2) and powder size distribution on the microstructure, phase content, hardness, porosity, oxidation and tensile adhesion of a cold work tool steel (X220CrVMo13-4) applied by HVOF. In this research, the powder size was classified into three different particle size ranges 25–45, 45–63 and 63–80 μm . Results showed that oxy-fuel ratio was the parameter with greater influence on creating low oxidation coatings, and medium powder size (45–63 μm) produced dense coatings with low oxidation.

The same cold work steel was investigated by Röttger et al. (Ref 34). In this study, the influence of particle size on the coating microstructure, phase content and coating porosity was determined for three particle size ranges 20–45, 45–63 and 63–80 μm . Smaller particles (20–45 μm) created a coating with higher oxide content and higher hardness. The amount of non-melted particles and porosity rise with the increase in particle diameter, along with the required heating of the particles to create enough deformation of the sprayed powder during impact. Due to the higher oxide content, the coating with smaller particles presented the lowest density among the coatings. Larger powder size (60–80 μm) presented a deficient heating of particles, resulting in a large amount of non-molten particles and a coating with little thickness.

Ajdelsztajn et al. (Ref 35) produced Fe-based amorphous HVOF coatings using two different particle size distributions (16–25 and 25–53 μm), in order to understand the particle size influence on the coating formation. Smaller particles (< 16 μm) probably experienced melting,

extensive deformation and severe oxidation. Larger particles (> 16 μm) do not reach the melting point but undergo extensive flattening and plastic deformation during impact, creating a coating with less oxidation and deformation of the particles.

This work presents the study of a FeCrMnSiB experimental alloy deposited by the HVOF thermal spray process onto SAE 1020 substrates. The main objective of this work is to determine how the particle size distribution and the presence of larger particles influence the oxide formation, morphology and cavitation resistance of the coatings. Larger particles are known to significantly reduce the oxide formation of the coatings. Therefore, a more detailed study of how the particle size distribution modifies the morphology, hardness, fracture toughness, cavitation resistance and mass loss mechanism of the sprayed coatings was chosen as subject for this paper.

Experimental Procedure

Coating Materials and Process

An experimental FeCrMnSiB alloy (66.1 wt.% Fe, 0.1 wt.% C, 15 wt.% Cr, 15 wt.% Mn, 0.30 wt.% N, 3 wt.% Si, 0.5 wt.% B) was used as feedstock powder and was deposited by high-velocity oxy-fuel (HVOF) process. This alloy is part of a research developed as part of a project with Instituto LACTEC and Copel Geração e Transmissão S.A., a research institute and an electric power generation company in the state of Paraná, Brazil. The goal of this project is deposit cavitation-resistant coatings using techniques that can reduce heat input to the substrate and the probability of crack formation in hydraulic runners.

The powder was prepared by inert gas atomization (ALD Vacuum Melting Induction System, Hanau, Germany) at Clausthal University of Technology (Clausthal-Zellerfeld, Germany). Atomized powder was sieved and separated in three particle size ranges: particles with maximum size of 45 μm (– 45 μm), particles with maximum size of 63 μm (– 63 μm) and particles within the range of 45 and 63 μm (+ 45–63 μm , which contains only particles larger than 45 μm and smaller than 63 μm). This particle size distribution was selected with the objective to observe how the presence of large particles (more than 45 μm) affects the microstructure and mechanical properties of the coatings.

HVOF coatings were deposited onto SAE 1020 carbon steel plates with dimensions of 35 × 75 × 8 mm (L × W × H). The surface was prepared by abrasive blasting to produce a surface free of impurities and with adequate surface roughness. Abrasive blasting parameters are given in Table 1. Coatings were deposited by HVOF

Table 1 Abrasive blasting parameters

Parameter	
Abrasive	White aluminum oxide #36 mesh
Method	Impingement with high pressure air
Air pressure, MPa	0.55-0.62
Blasting angle, °	90
Blasting distance, mm	150
Minimal roughness, μm	4.0 Ra

Table 2 HVOF parameters, (Ref 36)

Parameter	Value
Oxygen flow, m ³ /h	15.9
Propylene flow, m ³ /h	4.3
Air flow, m ³ /h	19.0
Powder feeding rate, g/min	45.0
Spray distance, mm	200
Coating thickness, μm	500

(Sulzer-Metco Diamond Jet2700, Pfäffikom, Switzerland) applied by Revesteel Company (Pinhais, PR, Brazil). The HVOF parameters, Table 2, were kept constant in order to not change the deposition condition of the coatings. The parameters were selected from a prior optimization (Ref 36) made for the HVOF deposition of FeMnCrSi+Ni+B coatings with particle diameter up to 63 μm, with the purpose of reducing the porosity and oxide content of the coatings. The coated samples were denominated as S-45 (with particles smaller than 45 μm), S-63 (with particles smaller than 63 μm) and S+45-63 (with particles between 45 and 63 μm). After the deposition of the coatings with the same parameters, different trials were realized observing the influence of the O₂/fuel ratio and spraying distance on the coatings deposited with the S-45 and S+45-63 powders.

The optimization of the parameters, shown in Table 3, had the objective to evaluate the influence of the O₂/fuel ratio and the spray distance on the morphology and properties of the coatings. The variation of these parameters was realized in accordance with the studies of Rajasekaran et al. (Ref 33) and Röttger et al. (Ref 34).

Characterization Methods and Evaluation

Prior to the powder sieving in the three considered ranges, a study of the atomized powder was performed by a particle size analyzer (CILAS 1064, Madison, USA) with limits of detection: between 0.04 and 500 μm to determine the particle size distribution. The morphological characterization of the powders, after sieving process, was

Table 3 HVOF parameters optimization for the powders S-45 and S+45-63

Parameter	Value
Oxygen flow, m ³ /h	12.7/19.1
Propylene flow, m ³ /h	3.4/5.2
Air flow, m ³ /h	19.0
Powder feeding rate, g/min	45
Spray distance, mm	150/200

performed by SEM—scanning electron microscopy (Tescan Vega 3, Brno, Czech Republic). The analysis of the powder phase content was made by XRD—x-ray diffraction (Shimadzu SDX 6000, Kyoto, Japan), with Cu target and Kα wavelength of 1.54 nm, working voltage of 40 kV, and 20 mA current. Scan speed of 1°/min and 0.02° step was used. Volume fraction of γ-Fe (austenite) and α'-Fe (martensite)/or δ-Fe (delta ferrite) was evaluated using the following equations (Ref 37, 38), measuring the intensities of (111)_γ and (110)_{α'} diffraction lines:

$$V_{\gamma} + V_{\alpha'} = 1 \tag{Eq 1}$$

$$V_{\gamma} = \frac{1.4I_{\gamma}}{I_{\alpha'} + 1.4I_{\gamma}} \tag{Eq 2}$$

where V_γ and V_{α'} are the volume fractions of γ-Fe and α'-Fe/or δ-Fe, respectively, and I_γ and I_{α'} are the intensities of (111)_γ and (110)_{α'} peaks, respectively.

Volume fraction of stress induced ε-Fe (martensite), γ-Fe (austenite) and α'-Fe (martensite)/or δ-Fe (delta ferrite) was evaluated using the following equations (Ref 39):

$$V_{\epsilon} = \frac{I_{\epsilon}}{0.67I_{\alpha'} + 0.89I_{\gamma} + I_{\epsilon}} \tag{Eq 3}$$

$$V_{\gamma} = \frac{0.89V_{\epsilon}I_{\gamma}}{I_{\epsilon}} \tag{Eq 4}$$

$$V_{\alpha'} = \frac{0.67V_{\epsilon}I_{\alpha'}}{I_{\epsilon}} \tag{Eq 5}$$

where V_ε, V_γ and V_{α'} are the volume fractions of ε-Fe, γ-Fe and α'-Fe/or δ-Fe, respectively, and I_ε, I_γ and I_{α'} are the intensities of (101)_ε, (111)_γ and (110)_{α'} peaks, respectively.

The characterization of the coatings morphology was performed by OM—optical microscopy (Zeiss A2.m, Oberkochen, Germany) and SEM. Porosity and oxide levels, as well as, the presence of other defects such as non-deformed particles, have been evaluated by analysis of the cross-sectional images, using a Axio Vision software. To determine the porosity and oxide content of coatings, the B test method of ASTM E2109-01 Standard (Ref 40) was followed. Chemical composition of the coatings was measured by EDS—energy-dispersive x-ray spectroscopy (x-act

Oxford Instruments, Abingdon, United Kingdom). Mechanical properties were measured by Vickers microhardness testing (Shimadzu HMV-G20, Kyoto, Japan) using the transversal section of the samples with a 0.98 N (100 g) of load, following ASTM E 384-11 Standard (Ref 41).

Indentation fracture toughness K_{IC} of the coatings was measured from the cross section of the coatings by Vickers microhardness testing (Shimadzu HMV-G20, Kyoto, Japan) with 19.61 N (2000 g) of load. Five indentations were carried on each coating. The Evans and Wilshaw equation (Ref 42) was used to calculate the fracture toughness:

$$K_{IC} = 0.079 \left(\frac{P}{a^{\frac{3}{2}}} \right) \log \left(\frac{4.5a}{c} \right) \quad (\text{Eq 6})$$

where K_{IC} is the fracture toughness ($\text{MPa m}^{1/2}$), P is the applied load (mN), a is half the diagonal of the indentation (μm), and c is the crack length measured from the center of the indentation (μm). This equation is valid for the range of $0.6 \leq c/a \leq 4.5$ (Ref 43), and thus, all results could be considered valid in this test.

Cavitation erosion tests were performed with vibratory (ultrasonic) cavitation equipment (Qsonica Q700, Newtown, USA) according to ASTM G32-03 Standard (Ref 44) in samples with dimensions of $25 \times 35 \times 8$ mm ($L \times W \times H$). Indirect method was carried out, with the specimen placed 500 μm from the tip of the sonotrode (tip diameter 19.0 mm). A peak-to-peak amplitude of 50 μm and frequency of 20 kHz were used, using distilled water maintained at 19 ± 1 °C. During cavitation erosion tests, the mass loss of the samples was measured (Shimadzu AUX 220). Cavitation mass loss behavior was investigated by SEM. Vickers microhardness tests were performed on the surface of the coatings with 2.94 N (300 g) of load, and cross-sectional region with 0.98 N (100 g) of load, before and after cavitation tests, in order to evaluate the strain hardening effect due cavitation erosion damage.

Results and Discussion

Powder Characterization

The powder particle size distribution is shown in Fig. 1. This study indicated that 65% of the particles are smaller than 45 μm and 82% are within the selected range of particle size for this study (less than 63 μm). This result shows the importance of the use of particles until 63 μm , which makes the study economically viable, since smaller particles add up to more than half of the total amount of powder. Moreover, the inclusion of the powder until 63 μm results in the use of almost every amount of powder, with a loss of 18%.

The morphological characterization of the powder by SEM is shown in Fig. 2. The particles presented spherical form, as expected. In the ranges of -45 μm (Fig. 2a) and -63 μm (Fig. 2b), a large portion of satellite particles was found. In the $+45$ - 63 μm range, the particles have a smaller variation of size with a significant content of satellite particles. Satellite particles are formed during the solidification by the joining of the smaller particles on bigger and hotter surface particles, as observed in Fig. 2(b).

The phase analysis of the atomized powders is given in Fig. 3. The XRD pattern, Fig. 3(a), identified the presence of the phases γ -Fe (austenite, FCC) and δ -Fe (delta ferrite, BCC) and/or α' -Fe (martensite, BCC) in the three studied particles size ranges. Figure 3(b) shows the volume fraction quantification of the identified phases for each particle size range, calculated by Eq 1 and 2. The powder with particle size of $+45$ - 63 μm contains a larger amount of γ -Fe phase (85.4%).

Similar behavior was found in the -63 μm powder, with 69.7% of γ -Fe phase and 30.3% of δ -Fe and/or α' -Fe phase. The -45 μm powder presented very similar amounts of γ -Fe and δ -Fe and/or α' -Fe phases (50.37 and 49.63%, respectively). These values indicate that larger particles have mainly austenite (γ -Fe), and smaller particles present larger amounts of δ -Fe and/or α' -Fe. δ -Fe is formed most likely due the rapid cooling of smaller particles during the atomization process, which can suppress the formation of the γ -Fe phase, and the primary δ -Fe structure is retained to room temperature (Ref 45). The α' -Fe martensite formation can also occur, because the γ -Fe \rightarrow α' -Fe transformation is facilitated by the chemical composition of the material, composed of elements (Mn, Si) that stabilize the austenite and also facilitate the martensitic transformation (Ref 46). Slower cooling rate of larger particles gives more time to promote the δ -Fe \rightarrow γ -Fe transformation. However, the presence of α' -Fe in this structure cannot be discarded, due to the common BCC structure between retained δ -Fe and α' -Fe. This leads to the formation of equal patterns in the XRD pattern, which makes it impossible to distinguish them only with this technique.

Coating Characterization

The characterization of the coatings showed different deposition efficiencies. The coatings S-45 and S-63 presented similar thickness per pass (11.4 ± 0.5 $\mu\text{m}/\text{pass}$ and 11.6 ± 0.28 $\mu\text{m}/\text{pass}$, respectively), while the S+45-63 coating presented a lower value of 9.4 ± 0.35 $\mu\text{m}/\text{pass}$. This indicates that the presence of smaller particles in the S-45 and S-63 coatings contributed to the adherence of the larger ones, which could not occur in the S+45-63 coating. Optimized parameters of the S-45 powders were obtained

Fig. 1 Laser dispersion: powder particle size distribution for the FeMnCrSiB powders

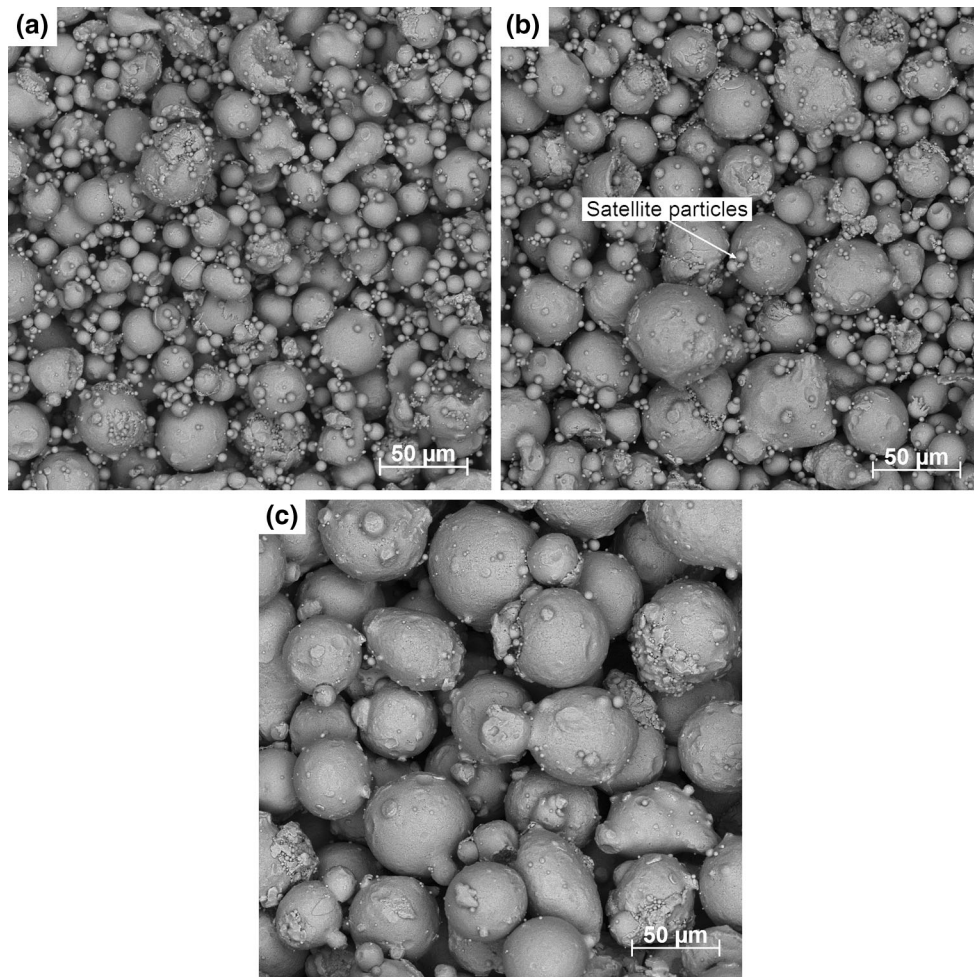
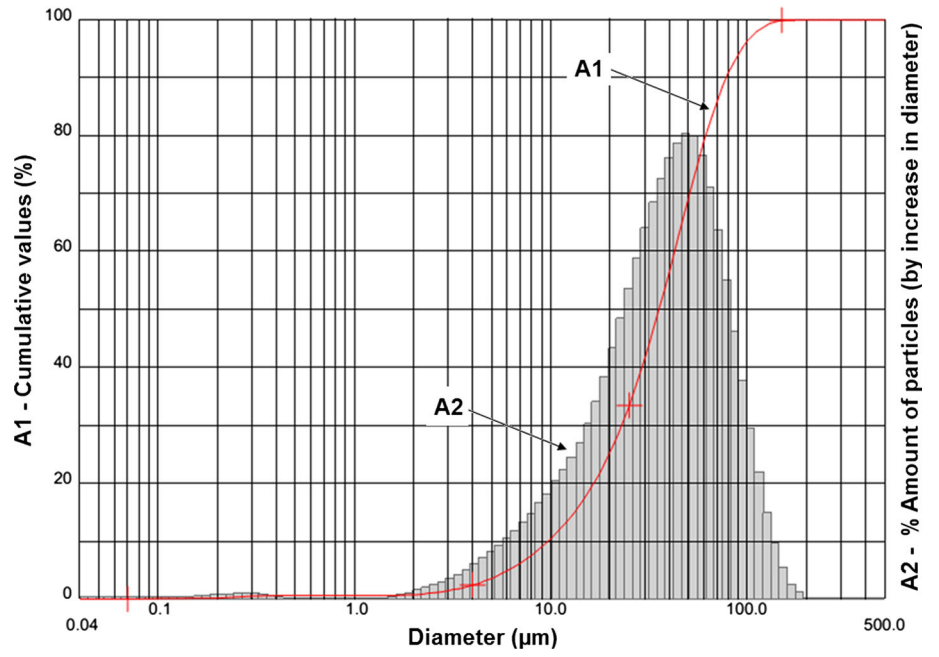


Fig. 2 SEM images: morphology of the atomized powder particles (a) – 45 μm, (b) – 63 μm and (c) + 45-63 μm, ×1000

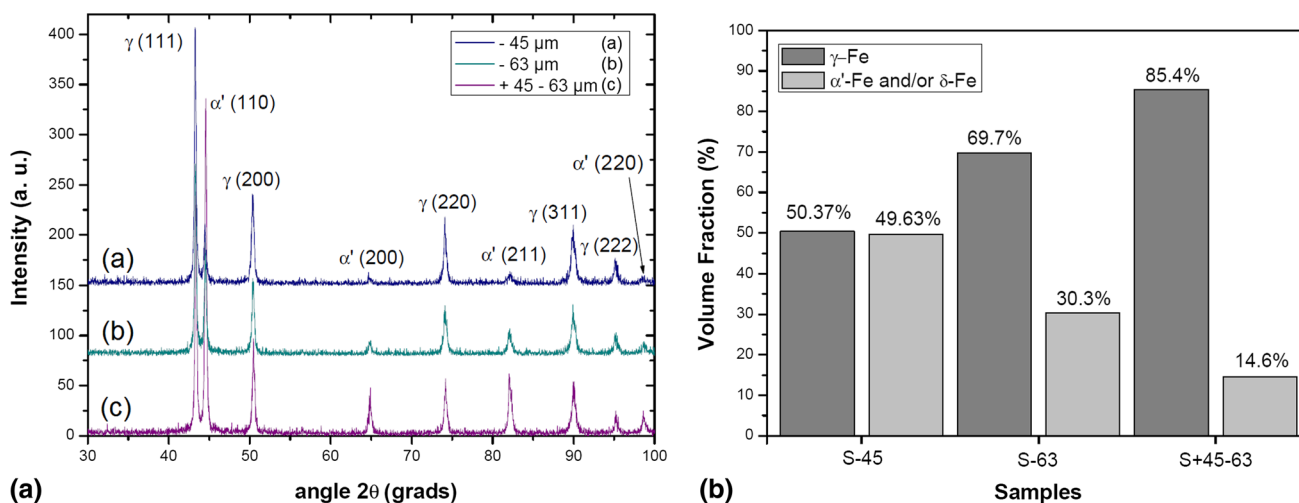


Fig. 3 Analysis of powders phase composition (a) XRD pattern and (b) results for phase volume fraction

by keeping the O_2 /fuel ratio and by using a shorter distance, minimizing the oxidation. For the S+45-63 powder, the optimized parameters were obtained by keeping the O_2 /fuel ratio in 3.7, but with the increase in the total gas flow. The oxygen flow was increased from 15.9 to 19.1 m^3/h and the propylene flow from 4.3 to 5.2 m^3/h , using a deposition distance of 200 mm. These optimized parameters promoted a slightly increase in the deposition efficiency of the S-45 powder to $12.5 \pm 0.5 \mu m/pass$; however, the deposition efficiency of the S+45-63 was not modified.

The microstructure of the HVOF coatings presented pores, oxides and molten or partially molten particles (identified as non-deformed particles) as shown in Fig. 4 and 5. Table 4 shows the oxide and porosity content of the coatings, measured by image analysis, and oxygen content, measured by EDS analysis. Oxygen content is directly correlated to a higher oxide content in the coatings, as observed by the values in Table 4. Oxide content is related to particle size, and smaller particles have more surface contact with the atmosphere, creating larger amount of oxides (Ref 34) and hence the greater oxide content in the S-45 sample. All samples presented low levels of porosity ($< 0.5\%$), which indicate a good deformation of particles to create the sprayed coating. As expected, S-63 and S+45-63 sample have lower oxide level S-45 sample, due to the presence of the higher size sprayed particles. As observed by previous authors (Ref 33, 34), an increase in the porosity with particle size rising is expected; however, these sample presented low level of porosity, despite the lesser deformation of particles. The low porosity of the coatings, even with the presence of large particles, can be explained by the presence of boron. Boron addition reduces the melting point of the alloy, which can contribute to the deformation of the particles. The reduction in the melting

point temperature with small boron addition was observed by Amushahi (Ref 47).

The reduction in spraying distance for the S-45 powder reduced the coating oxidation, as shown in Table 4 and Fig. 4 and 5, which is caused due to the particle temperature reduction, as previously discussed (Ref 48, 49) demonstrated for other materials. With a smaller particle size, the powder S-45 has a larger acceleration and consequently the velocity, at the moment of the impact, is probably equivalent to that of the S-63 powder with longer spraying distance (200 mm). For the S+45-63 powder, the enhance of the temperature and the velocity of the particles, increasing the total flow of gases, keeping the same O_2 /Fuel ratio, did not promote a significant alteration on the microstructure of the coating using this particle size. The increase in the temperature and velocity of the particles raising the total flow of fuel and oxygen gases was observed previously with NiCr powders on the work conducted by Oksa and Metsäjoki (Ref 50).

The presence of non-deformed particles indicates a lower degree of particle deformation. Larger particles tend to not reach enough speed and temperature required to deform, resulting in less deformation and deficient anchorage of the splats. Röttger et al. (Ref 34) also observed such behavior. According to previous study (Ref 25), maximum values of particle velocity and temperature, at the point of impact, correspond to particle sizes between 15 and 25 μm . Samples S-45 (refer to Fig. 4a) and S-63 (Fig. 4b) presented good particle anchorage. The presence of large particles, on the coating deposited with S-63 powder, increases the quantity of non-deformed particles, compared to sample S-45 sample. The coating deposited with S+45-63 (Fig. 4c) particles presented very high presence of non-deformed particles and consequently less anchorage of the splats in this sample. As observed by Li

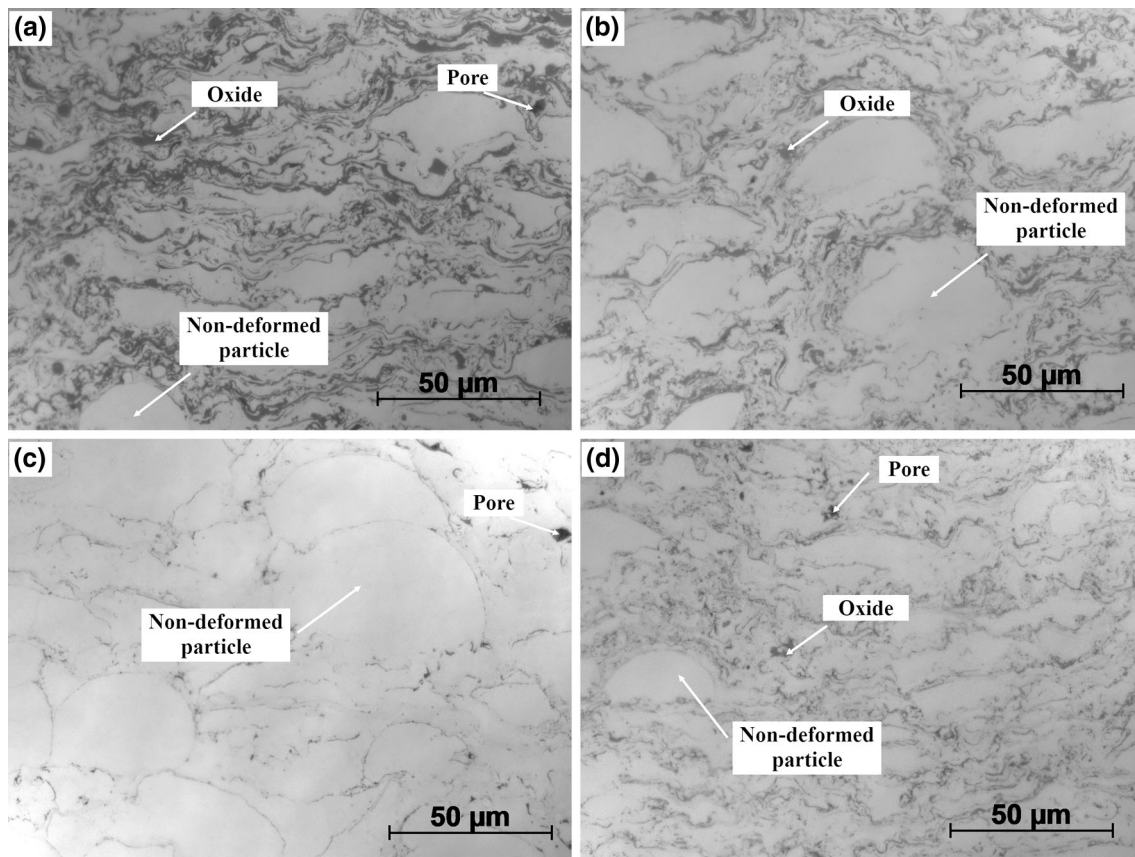


Fig. 4 OM Images: microstructure of the HVOF coatings, (a) S-45, (b) S-63, (c) S+45-63, (d) S-45 optimized, $\times 1000$

and Wang (Ref 51) in their work with HVOF, the melting state of metallic droplets changed with powder size, and the presence of large particle reduces the flattening of the droplets. They observed that the use of large particles increased the adherence of the coating; however, on the current research, the presence of larger droplets did not promote a splats adhesion increase, observed by the behavior of the fracture toughness.

For a more detailed phase analysis of the HVOF coatings, XRD measurements were carried out (Fig. 6). In comparison with the atomized powders, three new low intensity peaks are identified in Fig. 6(a), at 35.6° , 56.8° and $62.4^\circ 2\theta$. These peaks probably describe the presence of the following oxides: $\alpha\text{-Fe}_2\text{O}_3$ (Hematite) at 35.6° and $62.4^\circ 2\theta$ (Ref 52), and Mn_3O_4 (Manganese oxide) at $56.8^\circ 2\theta$ (XRD Reference Patter 00-013-0162). The S+45-63 coating did not present the above-mentioned peaks, most probably due to its low oxide content, reducing the possibility of XRD identification.

Figure 6(b) shows the volume fraction quantification of the identified phases for the samples, calculated by Eq 1 and 2. Results were similar with the previous powder results (Fig. 3b). Larger amount of $\gamma\text{-Fe}$ phase was found in

the S+45-63 sample (85.34%). Sample S-63 presented 57.08% of $\gamma\text{-Fe}$ phase and 42.92% of $\delta\text{-Fe}$ and/or $\alpha\text{-Fe}$ phase. The S-45 sample presented again very similar amounts of $\gamma\text{-Fe}$ and $\delta\text{-Fe}$ and/or $\alpha\text{-Fe}$ phases, but with larger quantity of the $\delta\text{-Fe}$ and/or $\alpha\text{-Fe}$ phases (50.55%).

Mechanical and Cavitation Erosion Properties

The mean average hardness of the studied coatings showed a maximum of $518.42 \pm 53.7 \text{ HV}_{100\text{gf}}$ for S-45 ($492.40 \pm 25.3 \text{ HV}_{100\text{gf}}$ for the sample deposited with shorter distance, because of the lower oxide content), followed by $485.3 \pm 72.86 \text{ HV}_{100\text{gf}}$ for S-63 and $314.25 \pm 96.52 \text{ HV}_{100\text{gf}}$ for S+45-63 (the hardness of the S+45-63 coating with higher volume of deposition gases showed similar values). Higher presence of oxides elevated the hardness of the S-45 sample. It was noted that the S+45-63 hardness values were significantly inferior to the other S-45 and S-63 samples, indicating that the presence of larger particles and almost no particle deformation and oxide content produced a coating of lower hardness. Besides, a greater presence of the $\gamma\text{-Fe}$ phase in this sample can be related to the lower hardness value.

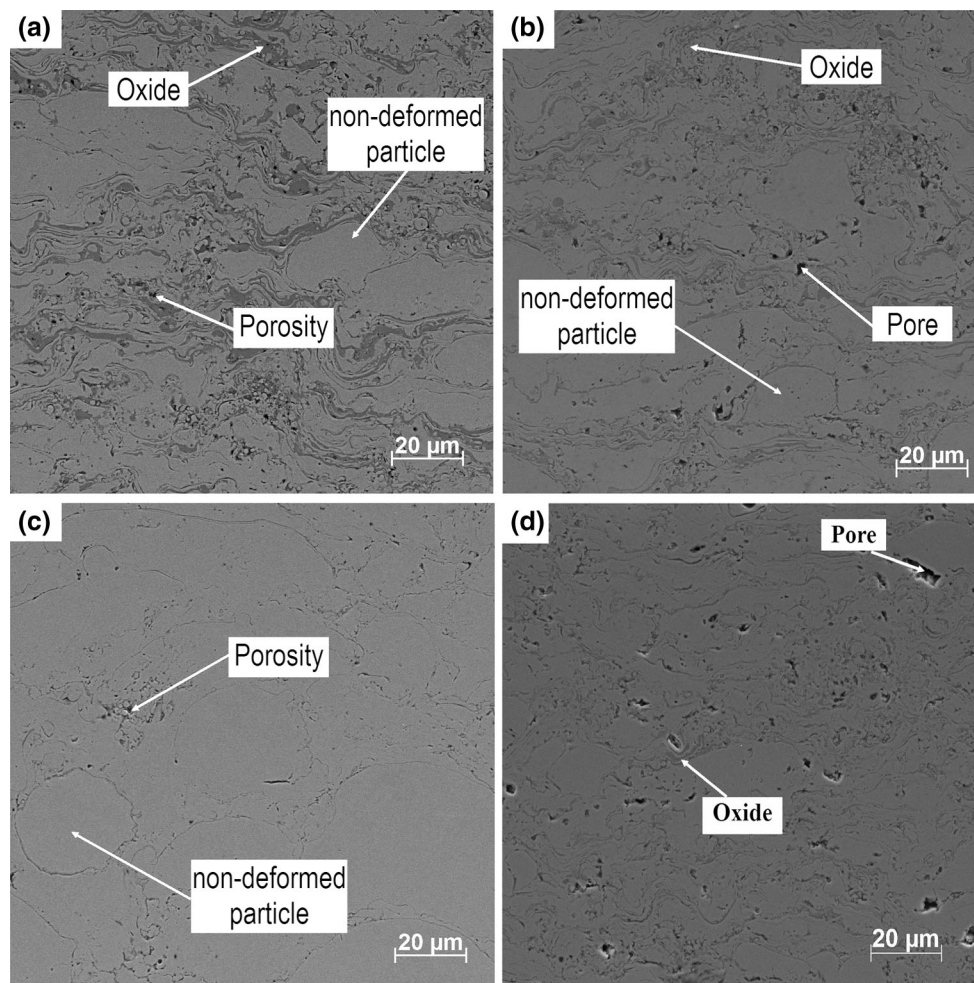


Fig. 5 SEM images: microstructure of the coatings, (a) S-45, (b) S-63, (c) S+45-63, (d) S-45 optimized, $\times 1000$

Table 4 Coating characteristics determined by image and EDS analysis

	Image analysis		EDS analysis
	Pore content, % area	Oxide content, % area	O, wt.%
S-45	0.04 ± 0.02	21.78 ± 3.67	7.6
S-63	0.07 ± 0.04	15.36 ± 1.21	5.6
S+45-63	0.16 ± 0.07	4.85 ± 0.94	0.8
S-45*	0.11 ± 0.12	11.81 ± 0.46	5.3
S+45-63*	0.32 ± 0.32	4.54 ± 0.61	0.8

S-45* and S+45-63* are the results after parameters optimization

Moreover, larger particles have inferior velocity, compared to smaller particles deposited with the same parameters (Ref 33). The impact of molten and partially molten particles at high velocity leads to the plastic deformation of the surface, resulting in the peening effect to the substrate. This leads to the creation of compressive stresses, which contribute to the increase in the adhesion of the coating to the substrate (Ref 29, 31). Higher cohesive strength of the coating has a linear dependence with hardness values of the

coatings, as observed in the literature (Ref 31). However, a previous research did not observe a clear correlation between the peening effect and the particle size (Ref 53). Such correlation is not so obvious that would relate the reduction of particle size and increase in velocity with higher formation of compressive stresses in the coatings.

Cross-sectional fracture toughness test of S-45 sample is shown in Fig 7. The results of the fracture toughness test of the coatings are shown in Fig. 8. The samples S-45 and

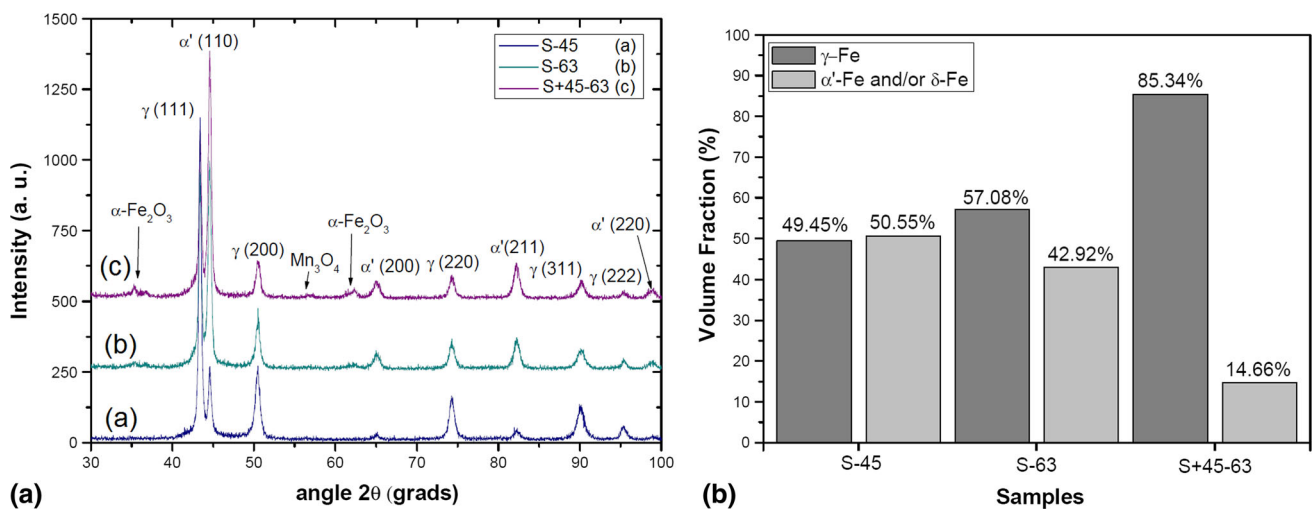


Fig. 6 (a) XRD pattern and (b) results for phase volume fraction of coatings after polishing

S-63 presented similar values of fracture toughness (2.6 and 2.4 MPa m^{1/2}, respectively). The sample S-45* deposited with 150 mm of spraying distance showed similar fracture toughness value, 2.5 MPa m^{1/2}. It was not possible to perform the fracture toughness test in the S+45-63 with higher gas flow, due to the thickness and porosity of the coating. The S+45-63 sample presented a value as low as half of the S-45 sample (1.36 MPa m^{1/2}). Previous research (Ref 43) correlated the cross-sectional fracture toughness with the cohesion properties of the lamella boundaries. The presence of heavy particles (15%) on the S-63 sample slightly reduces the fracture toughness of this coating, compared with S-45; nevertheless, the deposition of the S+45-63 coating with only heavy particles drastically reduces the fracture of the coating. This test confirms that larger particles reduced the intersplats adhesion due to the presence of non-deformed particles.

Cumulative mass loss results due to cavitation erosion tests are shown in Fig. 9. S-45 sample specimen showed better cavitation resistance, with an erosion rate of 7.8 mg/h, in comparison with 8.77 mg/h for S-63 and 20.26 mg/h for S+45-63 (Table 5). Total mass loss after ultrasonic cavitation tests showed a maximum of 83.8 mg for the S+45-63 sample. With shorter deposition distance, the powder S-45 showed a very similar behavior during cavitation test, as observed in Table 5. As opposed to S-45, the S+45-63 with higher gas flow showed a significant increase on its cavitation resistance, with erosion rate of 10.14 mg/h. Even with different deposition parameters, the coatings deposited with smaller powder particle size presented better cavitation resistance, which demonstrates the importance of its use.

The presence of smaller particles probably promotes better splats adhesion with a wettability increase, due to an increase in velocity and temperature of the smaller particles

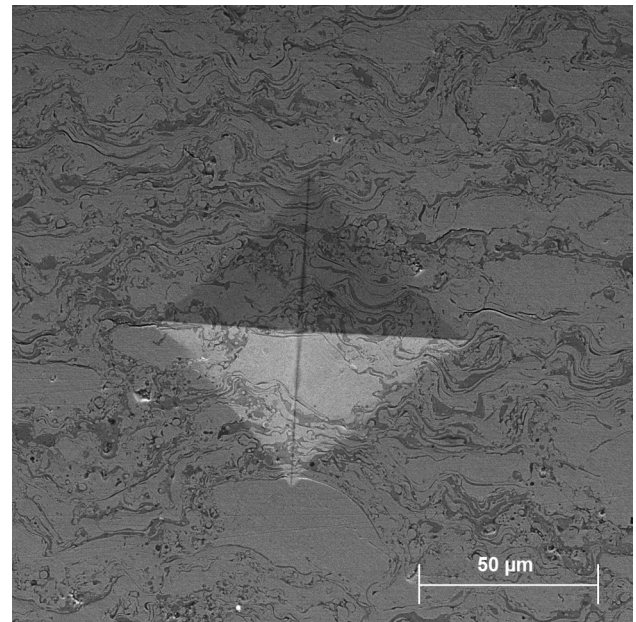


Fig. 7 Cross-sectional fracture toughness test indentation of the S-45 sample

(Ref 25). Initial mass loss (refer to detail in Fig. 9) shows that S+45-63 sample showed higher initial mass loss amounting to twice the initial loss of the other samples. The initial mass loss for all the samples increases quickly, which indicates that thermally sprayed coatings did not present an incubation period, as observed in the literature (Ref 28). The 1020 substrate is a bulk steel, and the incubation periods for bulk steels are in the 70–160 min range (Ref 28). In this study, the incubation period for the 1020 substrate was approximately 150 min, and the erosion rate, calculated after the incubation period, was 17.0 mg/h. Better adherence onto the substrate and between the coatings layers led to a coating twice as resistant to the

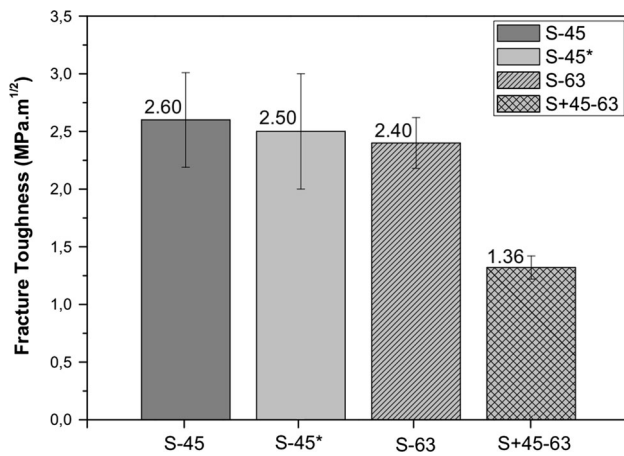


Fig. 8 Cross-sectional fracture toughness of the coatings

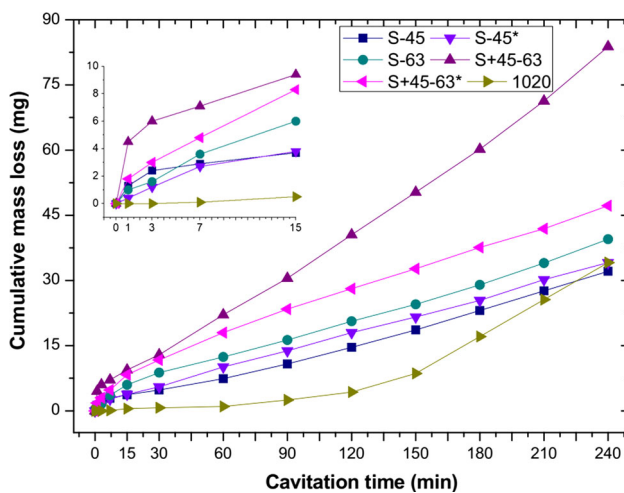


Fig. 9 Mass loss of coatings after ultrasonic cavitation tests

Table 5 Cavitation erosion rate of specimens tested (calculated after 30 min of tests)

Sample	Erosion rate, mg/h
S-45	7.8
S-63	8.77
S+45-63	20.26
S-45*	8.17
S+45-63*	10.14
1020 substrate**	17.0

**Calculated after incubation period (150 min)

cavitation erosion process, showing lower erosion rate values for the S-45 and S-63 samples.

The use of larger particles within the S-63 range did not impair the cavitation performance of the coating. The use of only larger particles with optimized parameters

presented better cavitation resistance than with the original parameters; however, it was still worse than the other coatings (S-45 and S-63). The economic factor also justifies the use of the powder until 63 μm , enabling the use of 82% of the powder produced by the atomization process.

Cavitation Erosion Mechanism

SEM images of the eroded surfaces enable a more detailed study and identification of the wear mechanisms during cavitation erosion tests, as presented in Fig. 10. The images were taken from the eroded areas at predetermined intervals (15, 30, 60 and 120 min). Cavitation erosion initiates at some preferable regions, like non-molten particles and surrounding the splats due to the proximity with pores (Ref 28) and oxide presence in these areas. The presence of non-deformed particles on the coating S+45-63, with low splats adhesion, observed by the lower values of the fracture toughness, accelerates the cavitation erosion when particles are entirely ripped off from the surface (Fig. 11). S+45-63 sample presented a higher presence of non-deformed particles, leading to the higher initial mass loss of this sample. After 120 min of test, an increase in erosion is observed in samples.

The XRD pattern of the coatings after cavitation test presented the stress induced ϵ -Fe (martensite) phase formation (Fig. 12a). Volume fraction of ϵ -Fe, γ -Fe and α -Fe phases (Fig. 12b) was calculated using Eq 3 to 5. The γ - ϵ transformation occurred by intense deformation of the surface due to the cavitation process. This transformation and hardness increase by work hardening during cavitation have a positive effect on the cavitation resistance of the coatings, absorbing the energy from the bubbles implosion (Ref 9). During the cavitation process, an energy absorption occurs by the metallic phase, and the cavitation damage can be absorbed mainly by the adhesion between the lamellae (interlamellar adhesion strength), and also by the phase transformation. The higher γ -Fe (austenite) content on the sample S+45-63 promotes an increase in the strain-induced phase transformation; with the presence of γ - ϵ transformation, it was not sufficient to minimize the mass loss.

Microhardness of the surface before and after cavitation test was performed to evaluate strain hardening. The microhardness of the HVOF coatings increased from $484.6 \pm 45 \text{ HV}_{300\text{gf}}$ to $780 \pm 159 \text{ HV}_{300\text{gf}}$ for the S-45 surface, and from $465.5 \pm 38 \text{ HV}_{300\text{gf}}$ to $817.8 \pm 131.7 \text{ HV}_{300\text{gf}}$ for the S-63 surface, indicating the strain hardening of the coatings. It was not possible to perform the tests in the S+45-63 sample, due to extremely high surface roughness after the cavitation tests. Strain hardening of the surface occurred due to the martensitic transformation, which was observed by the ϵ -martensite formation during the cavitation tests, verified by XRD analysis (Fig. 12).

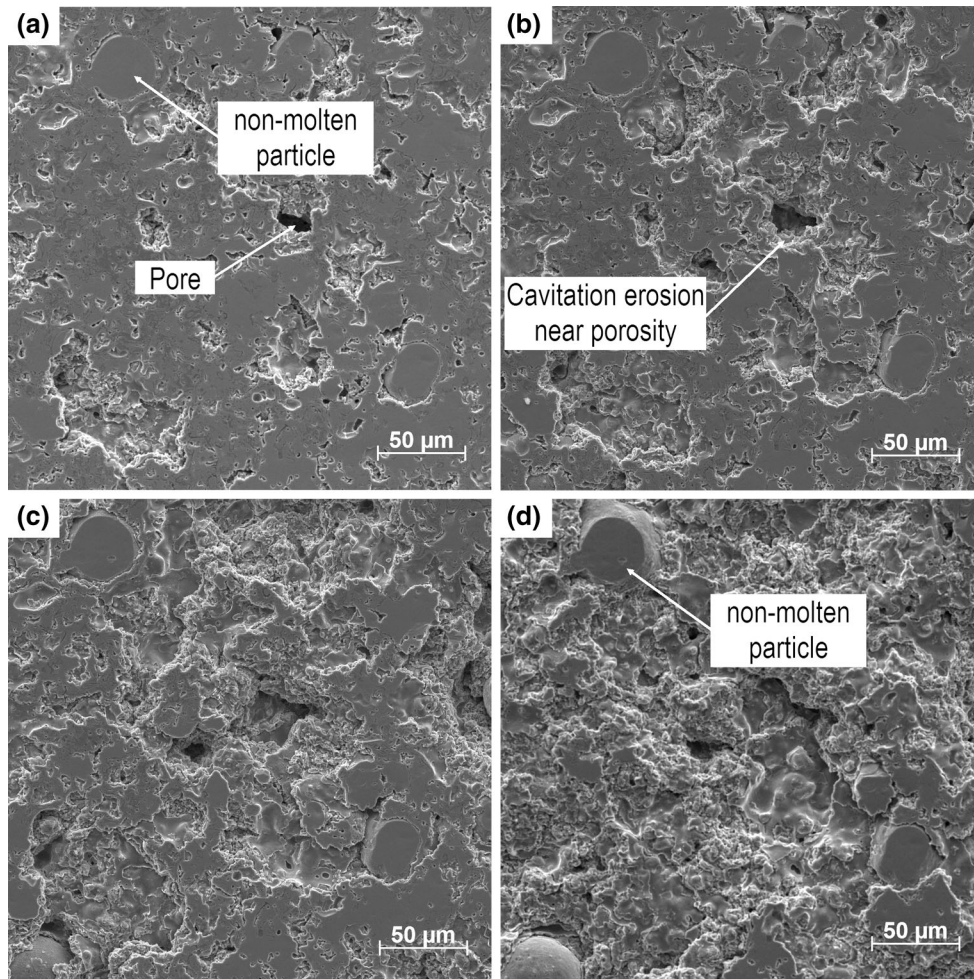


Fig. 10 SEM images, S-45 at (a) 15 min, (b) 30 min, (c) 60 min. and (d) 120 min of cavitation tests, $\times 500$

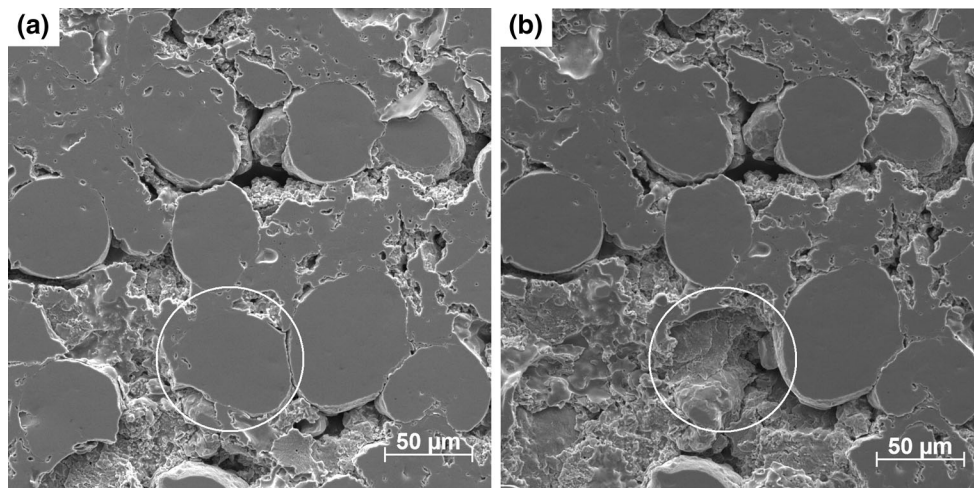


Fig. 11 SEM images, S+45-63 at (a) 15 min and (b) 30 min of cavitation tests, $\times 500$

The hardness increase in the S-45 and S-63 samples confirms the martensitic phase transformations by deformation on the surface of the coatings.

As a means of comparison, a cross-sectional Vickers hardness gradient of the coatings before and after the cavitation tests was performed, as shown in Fig. 13. It can

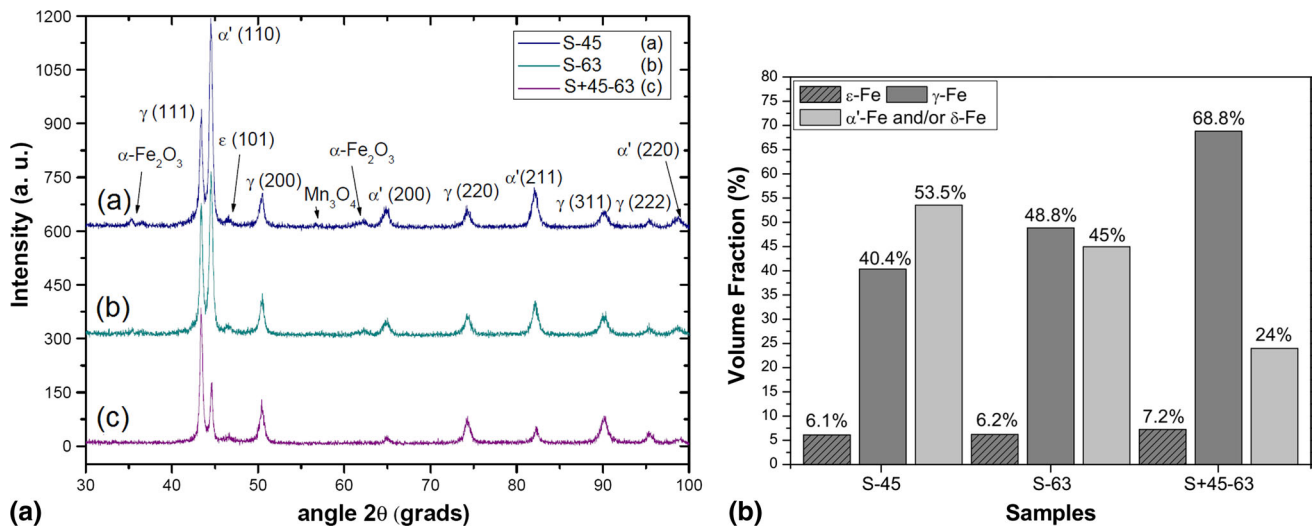


Fig. 12 (a) XRD pattern and (b) results for phase volume fraction of coatings after cavitation tests

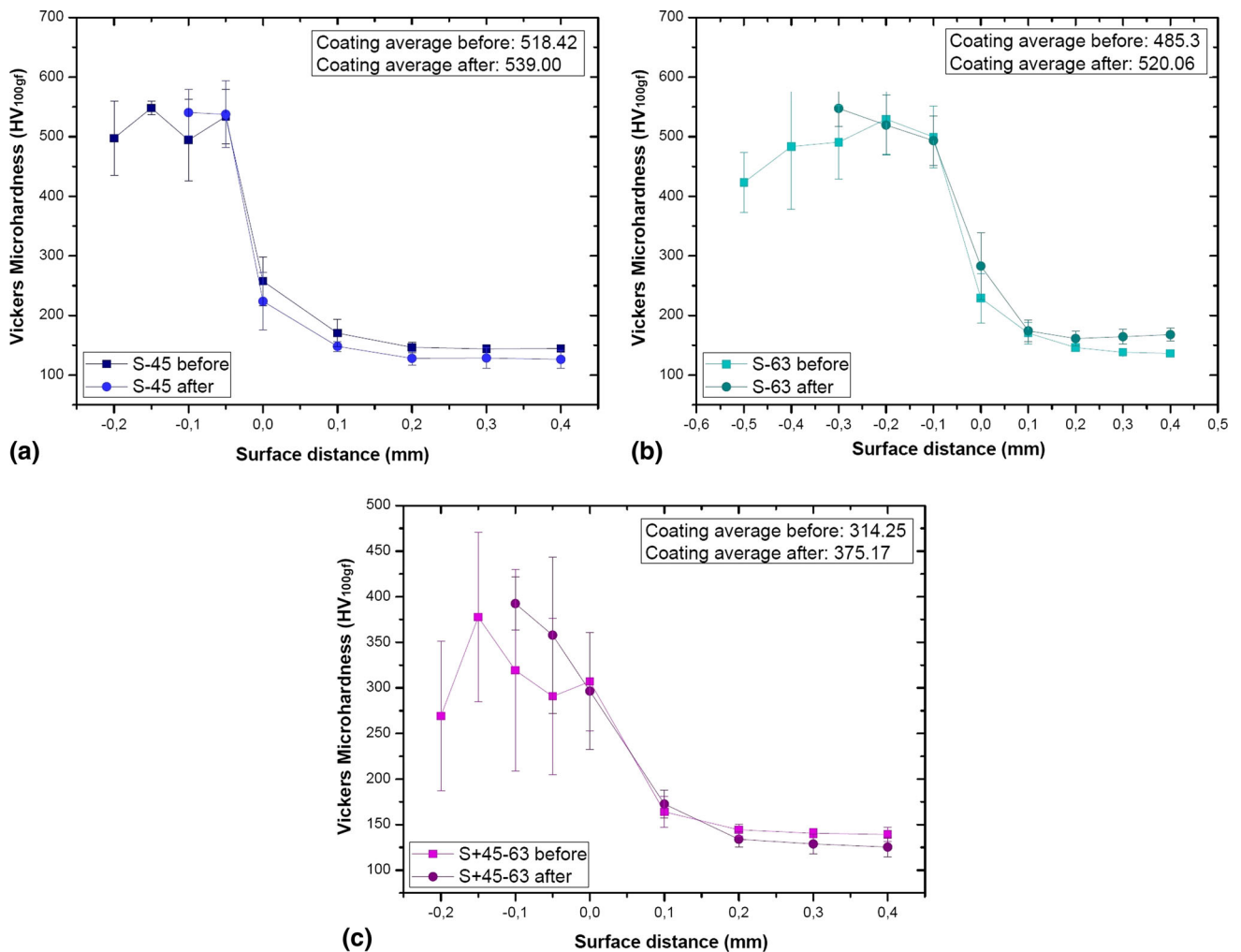


Fig. 13 Cross-sectional Vickers hardness before and after cavitation tests (a) S-45, (b) S-63, (c) S+45-63

be noted that all coatings presented an increase in the average hardness after cavitation tests (from 518.42 ± 53.7 to 539.00 ± 46.03 HV_{100gf} for S-45, from 485.3 ± 72.86 to 520.06 ± 45.18 HV_{100gf} for S-63 and from 314.25 ± 96.52 to 375.17 ± 63.75 HV_{100gf} for S+45-63), but this increase was inferior to that observed only in the surface of the coatings. Such behavior can be correlated with a located strain hardening of the coatings, which was not transmitted to the lower layers of the coatings. This resulted in a lower hardness average of the cross-sectional analysis after cavitation tests, when compared to the results of the test performed in the worn surface of the coatings, where the strain hardening is concentrated.

Conclusion

The influence of the presence of large particles on the morphology, porosity, oxide content, surface properties and cavitation resistance was studied in this work. It was observed that the presence of large particles had direct influence on the coating formation and cavitation resistance. The experimental findings are as follows:

1. XRD analysis of the atomized powders indicated the presence of γ -Fe (austenite) and δ -Fe (ferrite) and/or α' -Fe (martensite) in the three studied size ranges. However, the smaller particle size S-45 presents higher ferrite/martensite content. δ ferrite \rightarrow γ austenite transformation was affected by the particle size of the powder. Some γ -Fe \rightarrow α' -Fe transformation can occur mostly in smaller particles, due to rapid cooling.
2. The microstructure of the coatings presented small values of porosity, which indicates a good deformation of particles to create the sprayed coating. Oxide content was higher in the S-45 sample, due to the higher contact with oxygen by the smaller particles. The higher presence of non-deformed particles in the S+45-63 sample indicates lower fracture toughness and consequently the lower level of adhesion of the sprayed particles.
3. XRD patterns of the coatings showed low intensity peaks of the α -Fe₂O₃ (Hematite) and Mn₃O₄ (Manganese Oxide) oxide phases. Higher oxide content promotes an increase in the coatings hardness, as observed for the S-45 coating.
4. It was observed that S-45 specimen, deposited with lower quantity of heavy particles, showed the better cavitation resistance; meanwhile, S+45-63 sample presented higher mass loss. This is due to lower adhesion of the non-deformed particles, leading to a greater splats detachment.
5. The optimization of parameters allowed better deposition of larger particles (S+45-63). However, the use of the particle size range until 63 μ m, used in this article, allows the inclusion of particles adding up to 82% of the total particle amount, being more economically viable than the use of only smaller or larger particles.
6. SEM and XRD analysis showed strain hardening of the FeMnCrSiB coatings due to the γ - ϵ martensitic transformation, improving cavitation resistance, except for the case of the S+45-63 sample, which also presented the γ - ϵ martensitic transformation but suffered the higher cavitation erosion. Increase in hardness of S-45 and S-63 samples due to strain hardening was evaluated by microhardness testing, indicating the high level of strain hardening of the coatings.
7. The morphology of the coatings was the most important aspect for the higher resistance of the S-45 coating. Smaller particles created a coating with better splats adhesion and fracture toughness, and the erosion mechanism was concentrated surrounding the splats, with removal of its borders. The cavitation damage was absorbed mainly by the adhesion between the lamellae.

Acknowledgments The authors thank the Federal University of Technology Paraná, Ponta Grossa, Brazil (UTFPR-PG), the Thermal Spray and Special Welding Laboratory from Federal University of Paraná, Curitiba, Brazil (LABATS - UFPR), and the Institutos LACTEC, Curitiba, Brazil, for the availability of research structure. The Clausthal University of Technology, Germany, for the atomization of powder for this research. The Revesteel Metallization Company, Brazil, for the HVOF deposition. The Copel Geração e Transmissão S/A, for funding the research Project ANEEL PD-6491-0023/2010. The Coordenação de Aperfeiçoamento de Pessoal de Nível Superior (CAPES) for the provision of the scholarship, which assisted in the development of this work.

References

1. C.M. Hansson and L.H. Hansson, Cavitation Erosion, *ASM Handbook*, 1992, **18**, p 214-220
2. P.V. Marques and C.R.C. Lima, Studies of Cavitation Resistant Thermal Sprayed and Welded Coatings, in *Thermal Spray 2003: Advancing the Science and Applying the Technology*, 2003, **1**, p 389-393
3. J.H. Kim and M.H. Lee, A Study on Cavitation Erosion and Corrosion Behavior of Al-, Zn-, Cu-, and Fe-Based Coatings Prepared by Arc Spraying, *J. Therm. Spray Technol.*, 2010, **19**, p 1224-1230
4. W. Yuping, L. Pinghua, C. Chenglin, W. Zehua, C. Ming, and H. Junhua, Cavitation Erosion Characteristics of a Fe-Cr-Si-B-Mn Coating Fabricated by HVOF Thermal Spray, *Mater. Lett.*, 2007, **61**, p 1867-1872
5. L.A. Espitia and A. Toro, Cavitation Resistance, Microstructure and Surface Topography of Materials Used for Hydraulic Components, *Tribol. Int.*, 2010, **43**, p 2037-2045
6. J.P. Tullis and B.P. Tullis, Hydraulics of PIPE Systems, in *The CRC handbook of mechanical engineering*, 2005

7. X. Escaler, E. Egusquiza, M. Farhat, F. Avellan, and M. Cousirat, Detection of Cavitation in Hydraulic Turbines, *Mech. Syst. Signal Process.*, 2006, **20**, p 983-1007
8. R.L.P. Simoneau, Cavitation Erosion and Deformation Mechanism of Ni and Co Austenitic Stainless Steel, in *Proceedings of 7th Conference on Erosion by Liquid and Solid Impact*, 1987
9. Z. Wang and J. Zhu, Effect of Phase Transformation on Cavitation Erosion Resistance of Some Ferrous Alloys, *Mater. Sci. Eng. A*, 2003, **358**(1-2), p 273-278
10. S. Martin, C. Ullrich, D. Simek, U. Martin, and D. Rafaja, Stacking Fault Model of ϵ -Martensite and Its DIFFaX Implementation, *J. Appl. Crystallogr.*, 2011, **44**(4), p 779-787
11. F. Lecroisey and A. Pineau, Martensitic Transformations Induced by Plastic Deformation in the Fe-Ni-Cr-C System, *Metall. Mater. Trans.*, 1972, **3**, p 391-400
12. W.S. Lee and C.F. Lin, Impact Properties and Microstructure Evolution of 304L Stainless Steel, *Mater. Sci. Eng. A*, 2001, **308**(1-2), p 124-135
13. S. Allain, J.P. Chateau, O. Bouaziz, S. Migot, and N. Guelton, Correlations Between the Calculated Stacking Fault Energy and the Plasticity Mechanisms in Fe-Mn-C alloys, *Mater. Sci. Eng. A*, 2004, **387-389**, p 158-162
14. D.A. Woodford, Cavitation-Erosion-Induced Phase Transformations in Alloys, *Metall. Mater. Trans.*, 1972, **3**(5), p 1137-1145
15. M. Park, K. Kim, G. Shin, J. Yun, M. Shin, and S. Kim, Effects of Ni and Mn on the Cavitation Erosion Resistance of Fe-Cr-C-Ni/Mn Austenitic Alloys, *Tribol. Lett.*, 2013, **52**(3), p 477-484
16. J.Y. Yun, G.S. Shin, M.C. Park, H.S. Lee and W.S. Kang, Effect of Strain-Induced ϵ and α' -Martensitic Transformation on Cavitation Erosion Resistance in Austenitic Fe-Cr-C-MnFe-Cr-C-Mnti Alloys, *Wear*, 2015, **338-339**, p 379-384
17. F.T. Cheng, K.H. Lo, and H.C. Man, NiTi Cladding on Stainless Steel by TIG Surfacing Process Part I. Cavitation Erosion Behavior, *Surf. Coat. Technol.*, 2003, **172**, p 308-315
18. K. Jafarzadeh, Z. Valefi, and B. Ghavidel, The Effect of Plasma Spray Parameters on the Cavitation Erosion of Al_2O_3 - TiO_2 coatings, *Surf. Coat. Technol.*, 2010, **205**, p 1850-1855
19. R.K. Kumar, M. Kamaraj, S. Seetharamu, T. Pramod, and P. Sampathkumaran, Effect of Spray Particle Velocity on Cavitation Erosion Resistance Characteristics of HVOF and HVOF Processed 86WC-10Co4Cr Hydro Turbine Coatings, *J. Therm. Spray Technol.*, 2016, **25**(6), p 1217-1230
20. Z. Wang, X. Zhang, J. Cheng, J. Lin, and Z. Zhou, Cavitation Erosion Resistance of Fe-Based Amorphous/Nanocrystal Coatings Prepared by High-Velocity Arc Spraying, *J. Therm. Spray Technol.*, 2013, **23**, p 742-749
21. A.G.M. Pukaszewicz, P.R.C. Alcover, Jr., A.R. Capra, and R.S.C. Paredes, Influence of Plasma Remelting on the Microstructure and Cavitation Resistance of Arc-Sprayed Fe-Mn-Cr-Si Alloy, *J. Therm. Spray Technol.*, 2013, **23**, p 51-59
22. B. Kushner and E. Novinski, Thermal Spray Coatings, *ASM Handbook Vol. 18: Friction, lubrication and wear technology*, P.J. Blau, Ed., ASM International, Materials Park, 1992
23. L. Pawlowski, *The Science and Engineering of Thermal Spray Coatings*, Wiley, London, 1995
24. R. Kromer, J. Cormier, and S. Costil, Role of Powder Granulometry and Substrate Topography in Adhesion Strength of Thermal Spray Coatings, *J. Therm. Spray Technol.*, 2016, **25**, p 933-945
25. M. Li and P.D. Christofides, Feedback Control of HVOF Thermal Spray Process Accounting for Powder Size Distribution, *J. Therm. Spray Technol.*, 2004, **13**(1), p 108-120
26. K. Bobzin, M. Öte, T.F. Linke, and K.M. Malik, Wear and Corrosion Resistance of Fe-Based Coatings Reinforced by TiC Particles for Application in Hydraulic Systems, *J. Therm. Spray Technol.*, 2015, **25**, p 365-374
27. Y. Qin, Y. Wu, J. Zhang, S. Hong, W. Guo, L. Chen, and H. Liu, Optimization of the HVOF Spray Parameters by Taguchi Method for High Corrosion-Resistant Fe-Based Coatings, *J. Mater. Eng. Perform.*, 2015, **24**, p 2637-2644
28. G. Taillon, F. Pougoum, S. Lavigne, L. Ton-That, R. Schulz, E. Bousser, S. Savoie, L. Martinu, and J.-E. Klemberg-Sapieha, Cavitation Erosion Mechanisms in Stainless Steels and in Composite Metal-Ceramic HVOF Coatings, *Wear*, 2016, **364-365**, p 201-210
29. T. Varis, T. Suhonen, A. Ghabchi, A. Valarezo, S. Sampath, X. Liu, and S.-P. Hannula, Formation Mechanisms, Structure, and Properties of HVOF-Sprayed WC-CoCr Coatings: An Approach Toward Process Maps, *J. Therm. Spray Technol.*, 2014, **23**, p 1009-1018
30. T.C. Hanson and G.S. Settles, Particle Temperature and Velocity Effects on the Porosity and Oxidation of an HVOF Corrosion-Control Coating, *J. Therm. Spray Technol.*, 2002, **12**, p 403-415
31. M. Gaona, R.S. Lima, and B.R. Marple, Influence of Particle Temperature and Velocity on the Microstructure and Mechanical Behavior of High Velocity Oxy-Fuel (HVOF)-Sprayed Nanostructured Titania Coatings, *J. Mater. Process. Technol.*, 2008, **198**, p 426-435
32. D. Poirier, J.-G. Legoux, and R.S. Lima, Engineering HVOF-Sprayed Cr₃C₂-NiCr Coatings: The Effect of Particle Morphology and Spraying Parameters on the Microstructure, Properties, and High Temperature Wear Performance, *J. Therm. Spray Technol.*, 2012, **22**, p 280-289
33. B. Rajasekaran, G. Mauer, R. Vassen, A. Röttger, S. Weber, and W. Theisen, Coating of High-Alloyed, Ledeburitic Cold Work Tool Steel Applied by HVOF Spraying, *J. Therm. Spray Technol.*, 2009, **19**, p 642-649
34. A. Röttger, S.L. Weber, W. Theisen, B. Rajasekaran, and R. Vaßen, High Velocity Oxy Fuel Spraying of Cold Work Tool Steels—A Novel Approach to Thick Coatings for Wear Protection Applications, *Adv. Eng. Mater.*, 2009, **11**(12), p 1015-1022
35. L. Ajdelsztajn, J. Dannenberg, J. Lopez, N. Yang, J. Farmer, and E.J. Lavernia, High-Velocity Oxygen Fuel Thermal Spray of Fe-Based Amorphous Alloy: A Numerical and Experimental Study, *Metall. Mater. Trans. A*, 2009, **40A**, p 2231-2240
36. G.B. Sucharski, A.G.M. Pukaszewicz, R.F. Váz, and R.S.C. Paredes, Optimization of the Deposition Parameters of HVOF FeMnCrSi+Ni+B Thermally Sprayed Coatings, *Soldag. Insp.*, 2015, **20**(2), p 238-252
37. M. Tanaka and C.S. Choi, *Trans. ISIJ*, 1972, **12**, p 16-18
38. D.-S. Leem, Y.-D. Lee, J.-H. Jun, and C.-S. Choi, Amount of Retained Austenite at Room Temperature After Reverse Transformation of Martensite to Austenite in an Fe-13%Cr-7%Ni-3%Si Martensitic Stainless Steel, *Scr. Mater.*, 2001, **45**, p 767-772
39. I.M. Zylla, Gefügeoptimierung von metastabilen austenitischen Cr-Mn-Stählen zur Erhöhung der Kavitationsbeständigkeit durch verformungsinduzierte martensitische Umwandlung. Dissertation/PhD Thesis, 1991, VDI-Verlag GmbH.
40. I. Astm, ASTM E2109-2014, Standard Test Methods for Determining Area Percentage Porosity in Thermal Sprayed Coatings, 2014
41. I. Astm, ASTM E384-11, Standard Test Method for Knoop and Vickers Hardness of Materials, 2011
42. A.G. Evans and T.R. Wilshaw, Quasi-Static Solid Particle Damage in Brittle Solid. I. Observations Analysis and Implications, *Acta Metall.*, 1976, **24**, p 939-956
43. T. Varis, T. Suhonen, A. Ghabchi, A. Valarezo, S. Sampath, X. Liu, and S.P. Hannula, Formation Mechanisms, Structure, and Properties of HVOF-Sprayed WC-CoCr Coatings: An Approach Toward Process Maps, *J. Therm. Spray Technol.*, 2014, **23**(6), p 1009-1018

44. I. Astm, ASTM G32-03, Standard Test Method for Cavitation Erosion Using Vibratory Apparatus, 2003
45. A. Zambon, B. Badani, K. Eckler, F. Gärtner, A.F. Norman, A.L. Greer, D.M. Herlach, and E. Ramous, Microstructure and Phase Selection in Containerless Processing of Fe-Ni Droplets, *Acta Mater.*, 1998, **46**(13), p 4657-4670
46. D. Dunne, Shape Memory in Ferrous Alloys. In: E. Pereloma, D. Edmonds. Phase Transformations in Steel, Vol. 2: Diffusionless Transformations, High Strength Steels, Modeling and Advanced Analytical Techniques. *Woodhead Publishing*, 2012, p 83-125
47. M.H. Amushahi, F. Ashrafizadeh and F.M. Shamanian, Characterization of Boride-Rich Hardfacing on Carbon Steel by Arc Spray and GMAW Processes, *Surf. Coat. Technol.*, 2010, **204**(16-17), p 2723-2728
48. V.V. Sobolev and J.M. Guilemany, Investigation of Coating Porosity Formation During High Velocity Oxy-Fuel (HVOF) Spraying, *Mater. Lett.*, 1994, **18**(5-6), p 304-308
49. M.P. Planche, H. Liao, B. Normand, and C. Coddet, Relationships Between NiCrBSi Particle Characteristics and Corresponding Coating Properties Using Different Thermal Spraying Processes, *Surf. Coat. Technol.*, 2005, **200**(7), p 2465-2473
50. M. Oksa and J. Metsäjoki, Optimizing NiCr and FeCr HVOF Coating Structures for High Temperature Corrosion Protection Applications, *J. Therm. Spray Technol.*, 2015, **24**(3), p 436-453
51. C.-J. Li and Y.-Y. Wang, Effect of Particle State on the Adhesive Strength of HVOF Sprayed Metallic Coating, *J. Therm. Spray Technol.*, 2002, **11**(4), p 523-529
52. M.C. Morris, H.F. McMurdie, E.H. Evans, B. Paretzkin, H.S. Parker, and N.C. Panagiotopoulos, Standard X-ray Diffraction Powder Patterns Section 18: Data for 58 Substances, *Nat Bureau Stand. (U.S.) Monogr.*, 1981, **25**(18), p 37
53. S. Kuroda, Y. Tashiro, H. Yumoto, S. Taira, H. Fukunuma, and S. Tobe, Peening Action and Residual Stresses in High-Velocity Oxygen Fuel Thermal Spraying of 316L Stainless Steel, *J. Therm. Spray Technol.*, 2001, **10**(2), p 642-649